

## Heavy Quark Physics from SLD

Robert Messner\*  
Stanford Linear Accelerator Center  
Stanford University, Stanford, CA 94309

Representing the SLD Collaboration

### ABSTRACT

This report covers preliminary measurements from SLD on heavy quark production at the  $Z^0$ , using 150,000 hadronic  $Z^0$  decays accumulated during the 1993—1995 runs. A measurement of  $R_b$  with a lifetime double tag is presented. The high electron beam polarization of the SLC is employed in the direct measurement of the parity-violating parameters  $A_b$  and  $A_c$  by use of the left-right forward-backward asymmetry. The lifetimes of  $B^+$  and  $B^0$  mesons have been measured by two analyses. The first identifies semileptonic decays of  $B$  mesons with high  $(p, p_t)$  leptons; the second analysis isolates a sample of  $B$  meson decays with a two-dimensional impact parameter tag and reconstructs the decay length and charge using a topological vertex reconstruction method.

---

\*This work supported by the Department of Energy, contract DE-AC03-76SF00515 (SLAC).

## Introduction

The Stanford Linear Collider (SLC) together with the SLD Large Detector (SLD) provides an excellent facility for the study of the decay of the  $Z^0$ . The significant developments over the past year have been the most fundamental: the SLC has been able to deliver increased luminosity to the SLD detector at higher electron polarization. This progress is illustrated in Fig. 1, which shows the increase in the average polarization of the electron beam over time. During the 1993 running period, the SLD collected  $\sim 50,000$   $Z^0$  decays with a mean electron beam polarization of  $(63 \pm 1)\%$ . In 1994-1995, SLD recorded an additional  $\sim 100,000$  decays with a mean longitudinal polarization of  $(77 \pm 1)\%$ . Combined with the analysis advantage of a small, stable beam spot and the superior three-dimensional resolution of the SLD vertex detector, this data set has provided accurate measurements of fundamental electroweak parameters. We will cover preliminary results for a set of topics SLD has studied involving heavy quark physics. These include a measurement of  $R_b$ , heavy quark asymmetries, and a measurement of B meson lifetimes utilizing two analysis methods.

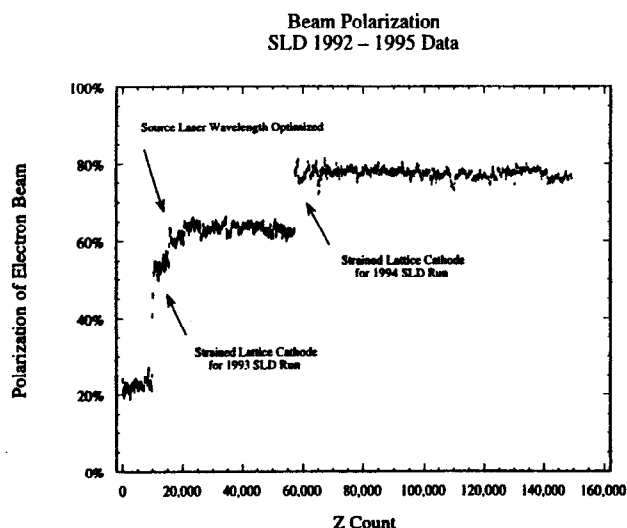


Figure 1. A summary of the beam polarization and the  $Z^0$  decays recorded by the SLD.

A side view of the SLD is given in Fig. 2; the interaction between the SLC and the SLD and the production and measurement of the electron beam polarization are covered in the talk by T. Schalk in these proceedings.

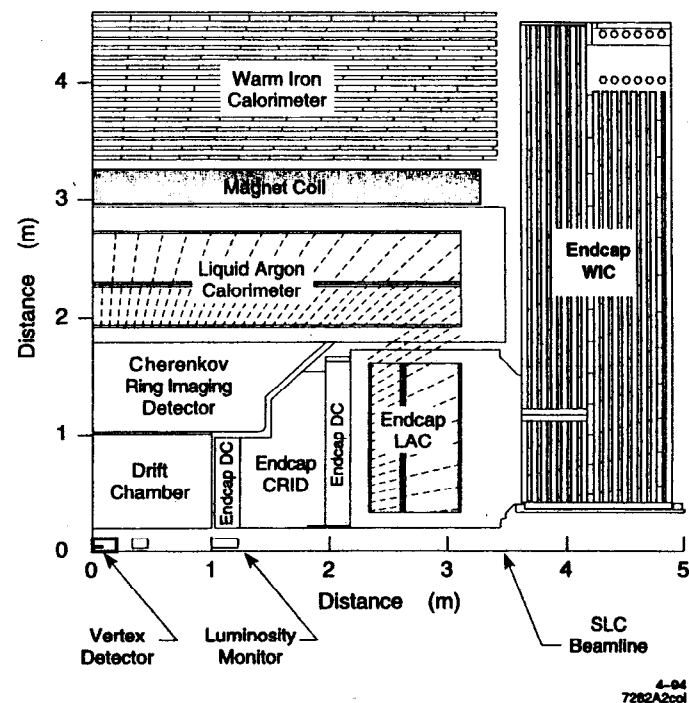


Figure 2. A quadrant of the SLD detector.

## The SLD Detector

A detailed description of the SLD detector can be found in Ref. [1]. Working from the interaction point (IP) outward, the detector incorporates a vertex detector (VXD) for precise position measurements close to the interaction region, a central drift chamber (CDC) for charged particle tracking and momentum measurements, a Cherenkov ring imaging detector (CRID) for particle identification, a liquid argon calorimeter (LAC) for measuring energy flow and providing electron identification, the solenoid coil, and the warm iron calorimeter (WIC), which provides the magnetic field flux return and muon identification, and serves as a tail catcher for hadronic showers extending beyond the LAC.

Together, the VXD and the CDC provide the core of the SLD tracking measurements used in the analyses to be discussed later.<sup>2</sup> The VXD consists of 480 charge-coupled devices (CCD's) surrounding a 1 mm thick beryllium beam pipe with an inner radius of 25 mm. Each CCD is an array of  $375 \times 578$  square pixels  $22 \mu\text{m}$  on a side. The

CCD's are arranged in four concentric cylinders at radii ranging from 2.9 cm to 4.1 cm. The inner (outer) cylinder covers a range of polar angles defined by  $\cos\theta < 0.85$  (0.75). The CDC is a cylinder 1.8 m long with an inner radius of 0.2 m and an outer radius of 1.0 m. Six hundred and forty drift cells are arranged in ten superlayers covering radii from 24 cm to 96 cm. Each cell in a superlayer has eight sense wires spaced radially by 5 mm. An individual sense wire provides a measurement of the drift distance with a spatial resolution averaging  $70\ \mu\text{m}$  over the entire drift cell. Tracks are reconstructed at polar angles in the range  $\cos\theta < 0.85$ .

The capabilities of the VXD are summarized in Figures 3 and 4. Figure 3 displays the measured miss distance between the two tracks of muon pairs obtained from decays of the  $Z^0 \rightarrow \mu^+\mu^-$ . Since the two muons originate from a common point, this is a good measure of the intrinsic resolution for an individual track's impact parameter relative to its origin; the width of the distribution is divided by  $\sqrt{2}$  because there are two tracks used to make the measurement. Correcting for this, the resolution in the  $r$ - $\phi$  plane is found to be 11.2 microns, and in the  $r$ - $z$  plane 37 microns.

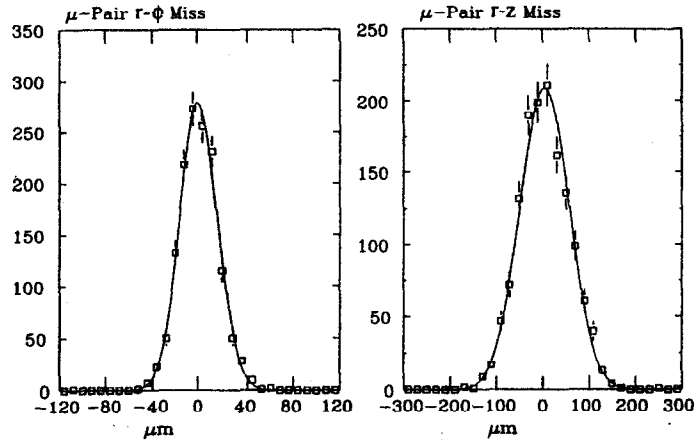


Figure 3. The miss distance between muons in the  $r$ - $\phi$  and  $r$ - $z$  planes.

Figure 4 demonstrates the accuracy of the beam spot determination. It plots the impact parameter for individual muon tracks, again from  $Z^0 \rightarrow \mu^+\mu^-$  pairs, relative to the position of the IP in the  $r$ - $\phi$  plane. The IP position is determined independently from hadronic events. The width of the distribution is 12.9 microns. Unfolding the intrinsic impact parameter resolution of the tracks, we find the accuracy for the IP spot determination to be 6.4 microns.

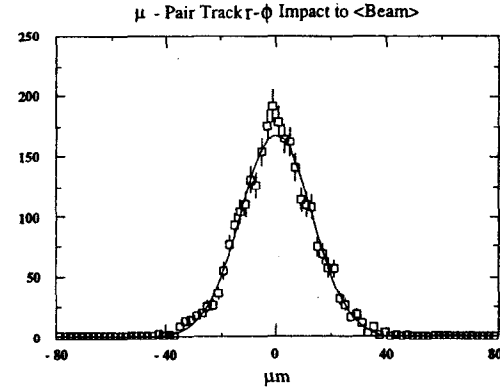


Figure 4. The impact parameter for muons relative to the IP.

### Couplings of Fermions to the $Z^0$

The Standard Model (SM) makes definite predictions for a number of attributes of  $Z^0$  decays, making possible precision tests by comparing these with the experimental values. Possible new physics beyond the SM may make itself manifest through radiative corrections to the SM couplings. An elegant and thorough review of the status of world measurements and the implications for the SM is given in the lectures by M. Swartz in these proceedings (see also Ref. [3]). We concentrate here on couplings of the  $Z^0$  to heavy quarks. Tests using measurements of heavy quark production, especially that of the  $b$  quark, are primarily sensitive to corrections at the  $Z^0 \rightarrow f\bar{f}$  vertex. This is distinct from measurements of  $\sin^2\theta_w$ , such as the electron asymmetry or tau polarization asymmetry, which are tests sensitive to corrections that involve the  $Z^0$  propagator. The two types of measurements complement one another in the nature of their probing of the SM.

### $R_b$ : Lifetime Double Tag

A quantity of particular current interest is the branching fraction of the  $Z^0$  into  $b$  quarks. Significant top mass corrections are expected to affect the cross section for  $Z^0 \rightarrow b\bar{b}$ . The best experimental quantity to compare with predictions is  $R_b$ , the ratio  $\Gamma(Z^0 \rightarrow b\bar{b}) / \Gamma(Z^0 \rightarrow \text{hadrons})$ . In this ratio, most corrections excepting vertex corrections cancel, so that the theoretical ambiguities are relatively small. Moreover, because the vertex corrections are isolated, the predicted value of  $R_b$  becomes a function of the top mass, again with little uncertainty. The ratio has the additional advantage that experimental uncertainties tend to cancel as well. LEP has made measurements of  $R_b$  using several techniques, and their current average is  $3\sigma$  high compared to the SM. (See the talk by D. Strom in these proceedings for a current review of the LEP measurements.)

The SLD measurement of  $R_b$  employs a lifetime double-tag technique similar to the ALEPH measurement.<sup>4, 5</sup> The primary difference lies in the intrinsic resolution of the vertex detector, including its three-dimensional information, and the size of the interaction region. The information of the IP position is utilized in the following manner. After a selection of  $Z^0$  decays has been made, each event is divided into two hemispheres using the direction of the highest momentum jet as the axis. Track parameters are computed using only the information from the VXD and CDC systems; a second analysis of each track is made by adding the beam spot position as an extra hit on the track. A variable,  $\chi$ , is defined which represents the difference in the square root of the chi-squared of the fit track for the two computations. This is equivalent to the normalized three-dimensional impact parameter to the primary vertex for each track. Tracks that originate close to the IP will have a small value of the impact parameter. Tracks that originate further from the IP, such as those originating from decays of heavy quarks, will have a large value. An additional refinement is made by assigning a sign to  $\chi$  depending upon whether the point of closest approach of the track to the axis of the highest momentum jet is in the same hemisphere ( $\chi$  positive) or the opposite hemisphere ( $\chi$  negative) as the track itself.

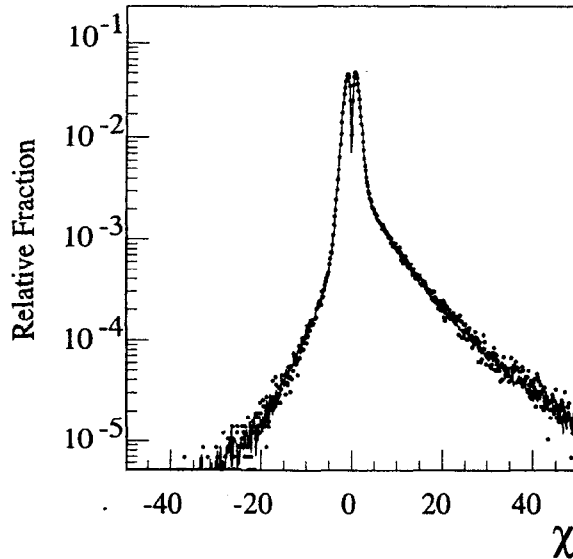


Figure 5. The  $\chi$  distribution for data and Monte Carlo.

A plot of  $\chi$  compared with Monte Carlo is shown in Fig. 5. The dip at the origin is due to the lack of phase space for tracks to point exactly at the IP in three dimensions. In the region of positive  $\chi$ , a tail can be seen at the larger values; these tracks are predominately from particles decaying far from the IP. Decays of particles containing heavy quarks dominate this region. The probability that an individual track originated

from the primary vertex is then computed using the shape of the distribution of negative  $\chi$ , reflected about the origin, for the template. The next step is to look at the ensemble of tracks in a particular hemisphere. Only tracks with positive  $\chi$  are kept. A joint probability, that the ensemble of tracks in a hemisphere is consistent with coming from the IP, is then formed using a Poisson  $\chi^2$  probability distribution.

Hemispheres with a low joint probability represent a data sample enriched in  $b$  decays. A cut on the joint probability is then made;  $b$  decays are isolated by requiring that events have a joint probability below the value of the cut. Figure 6 shows a plot of the purity,  $\Pi_b$ , of the resultant  $b$  sample and the efficiency,  $\epsilon$ , for the different quark species as a function of the value used for the cut. The precise value of the cut is determined by that value which minimizes the total error of the resultant data sample for measuring  $R_b$ .

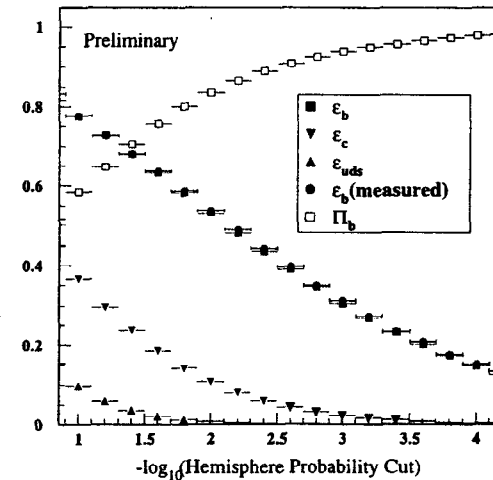


Figure 6. The purity,  $\Pi_b$ , and efficiency,  $\epsilon_b$ , of the  $b$  sample as a function of the cut on the log of the hemisphere joint probability.

Knowledge of the efficiency for tagging  $b$  events is crucial for determining  $R_b$ . Note that Fig. 6 has two values plotted for  $\epsilon_b$ . One is determined purely by Monte Carlo, while the other has been determined from the data by comparing the number of hemispheres tagged as containing a  $b$  quark with the number of events for which both hemispheres are so tagged. One would like the efficiency to be determined completely by the data if so possible. In a perfect world, if there were no background so that the  $b$  tags represented a pure  $b$  quark sample and the tagging of either of the two hemispheres was independent of the other,  $R_b$  and the efficiency,  $\epsilon_b$ , could be obtained by solving the following two simultaneous equations:

$$n_{\text{hemi}} = 2\varepsilon_b R_b N_{\text{event}} \text{ and } n_{\text{double}} = \varepsilon_b^2 R_b N_{\text{event}}.$$

In practice, however, non-b related backgrounds are present and their effect must be included. Similarly, the tagging efficiency of the two hemispheres has a nonzero degree of correlation between them due to a number of causes; a simple example would be the acceptance of the detector, while others include the effects of gluon radiation or small errors in the determination of the IP position. The correlation likewise must be accounted for. The resultant equations are more complicated, but  $R_b$  and  $\varepsilon_b$  can still be extracted with input from the Monte Carlo for the values of  $\varepsilon_{\text{uds}}$ ,  $\varepsilon_c$ , and the correlations between hemisphere efficiencies, and assuming a SM value of  $R_c = 0.171$ .

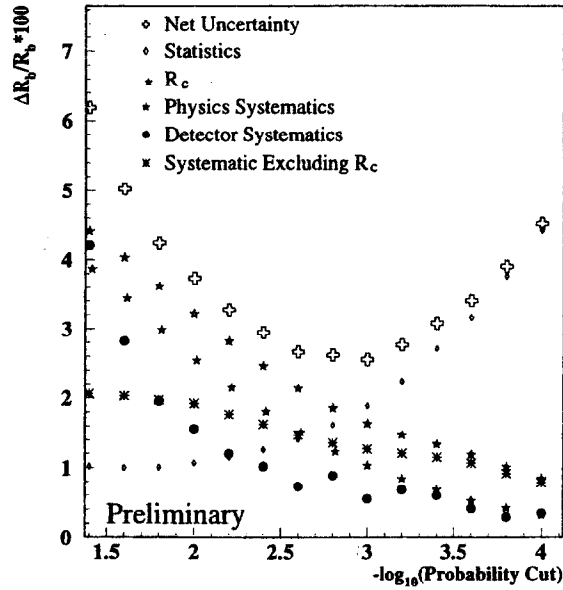


Figure 7. The uncertainty in  $R_b$  as a function of the cut on the log of the hemisphere joint probability.

The systematic and statistical errors for the value of  $R_b$  extracted from the data set are shown in Fig. 7. The choice of the value for the cut on the joint probability is set at the minimum in the curve for the net uncertainty in the value of  $R_b$ . This represents a balance between the statistics of the final sample and the systematic errors of the analysis. The variation in the result for  $R_b$  as the cut is changed is shown in Fig. 8; the flatness of this curve gives us confidence in the stability of the result.

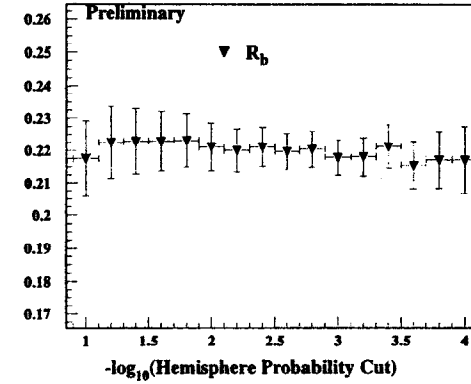


Figure 8. The dependence of the result for  $R_b$  upon the value of the cut on the log of the hemisphere joint probability.

The minimum combined systematic and statistical uncertainty occurs at a hemisphere joint probability cut of  $10^{-3.0}$ . The efficiency  $\varepsilon_b$  for this cut measured from data is  $31.3 \pm 0.6\%$ , with a b-tagging purity  $\Pi_b$  of 94%. The preliminary result for  $R_b$  is

$$R_b = 0.2171 \pm 0.0040 \text{ (stat)} \pm 0.0037 \text{ (sys)} \pm 0.0023 \text{ (} R_c \text{)}.$$

The value is consistent with the expectation of the SM. The SLD result is not yet precise enough either to certify or to de-certify the  $3\sigma$  discrepancy currently observed by the LEP experiments.

Table 1

Systematic Source	$\delta R_b/R_b$	Systematic Source	$\delta R_b/R_b$
Correlation Systematics		Charm Systematics	
B lifetime	0.03%	D lifetime	0.15%
B-decay multiplicity	0.14%	D-decay multiplicity	0.87%
B $\rightarrow$ D model	0.02%	c $\rightarrow$ D fractions	0.57%
b fragmentation	0.30%	c fragmentation	0.56%
$\Lambda_b$ fraction	0.31%	$R_c = 0.171 \pm 0.017$	1.05%
MC statistics	0.41%	MC statistics	0.26%
Light quark systematics		Detector systematics	
K, $\Lambda$ production	0.04%	$V^0$ rejection	0.85%
$g \rightarrow c\bar{c}, b\bar{b}$	0.19%	Tracking efficiency	0.41%
MC statistics	0.11%	Impact resolutions	0.35%
		Beam position tails	0.29%

A breakdown of the sources of the systematic error is given in Table 1. The largest contributors are seen to lie in the charm sector. Note that the systematic error due to the uncertainty in the value for  $R_c$  has been isolated. Improvements in techniques to remove charm decays will be a key to reducing systematic errors. Further gains in this analysis will require the development of an efficient, ultra-high purity b-tag to improve systematics in hand with a larger sample of data.

### $Z^0$ Asymmetries at the SLD

In the SM, fermions have vector and axial vector couplings  $v_f$  and  $a_f$  to the  $Z^0$ . The asymmetries at the Z-pole depend on the vector-axial vector interference term. Conventionally, one defines for each fermion the quantity

$$A_f = \frac{2v_f a_f}{v_f^2 + a_f^2}.$$

The asymmetries one has access to experimentally involve different combinations of the  $A_f$  relevant to a particular process (see M. Swartz, these proceedings.) The advantage of the high polarization of the incident electron beam at the SLC is that it enables us to separate the electron coupling from the fermion coupling to the  $Z^0$ .<sup>6</sup> As an example, one can look at the expression for the left-right forward-backward asymmetry  $\tilde{A}_{FB}^f$ . This is written below for the b quark:

$$\tilde{A}_{FB}^b = \frac{[\sigma_L(F) - \sigma_L(B)] - [\sigma_R(F) - \sigma_R(B)]}{[\sigma_L(F) + \sigma_L(B) + \sigma_R(B) + \sigma_R(F)]} = \frac{3}{4} P_e A_b.$$

F (B) denotes an outgoing fermion that goes in the same (opposite) direction as the incident electron.  $\sigma_L$  ( $\sigma_R$ ) is the cross section for left (right) polarized electrons colliding with (unpolarized) positrons. Besides providing a means to measure  $A_b$  directly, the use of  $\tilde{A}_{FB}^b$  has the practical effect of enhancing the analytical power of the events used for the measurement relative to a measurement of the unpolarized forward-backward asymmetry  $A_{FB}^b$ . This is because the unpolarized forward-backward asymmetry has the quantity  $A_e$  rather than  $P_e$  multiplying the final state fermion term:

$$A_{FB}^b = \frac{3}{4} A_e A_b.$$

Since  $A_e$  is small, the relative statistical sensitivity of the two methods,  $(P_e / A_e)^2$ , becomes quite large for a highly polarized beam; for the SLD, the enhancement we gain by eliminating the electron coupling is on the order of 25.

The expression for  $\tilde{A}_{FB}^f$  above is obtained by integrating the Born-level differential cross section:

$$\frac{\partial \sigma_f}{\partial \cos \theta} \propto (1 - A_e P_e) \left( \frac{1 + \cos^2 \theta}{2} + A_f \left( \frac{A_e - P_e}{1 - A_e P_e} \right) \cos \theta \right).$$

Here,  $\theta$  is the angle between the incoming  $e^-$  and the outgoing fermion  $f$ . The direction of the thrust axis can be used to determine the direction of the outgoing fermion. The sign of  $P_e$  in the differential cross section can also be manipulated to give the left-right forward-backward asymmetry as a function of  $\cos \theta$ :

$$\tilde{A}_{FB}^f(\cos \theta) = |P_e| A_f \frac{2 \cos \theta}{1 + \cos^2 \theta}.$$

One needs, in addition to providing a polarized incident electron beam, to select a sample of events enriched in a particular quark flavor and to tag the direction of the quark versus the antiquark to determine if an event is a forward or a backward event.

The majority of the analyses to follow use the full Born-level differential cross section in making the fits. The use of the full form for the cross section in fitting the data allows the analysis to include corrections and detector effects in a more thorough and straightforward manner, while maintaining the ability to eliminate the dependence on the electron coupling as discussed above.

### Measurement of $A_c$ Using $D^{*+}$ and $D^+$

This is an update of the measurement made with the 1993 data.<sup>7</sup> In order to tag  $c\bar{c}$  events and separate them from  $b\bar{b}$  and  $uds$  backgrounds, kinematic and vertex analyses are used to find events containing one of two  $D^{*+} \rightarrow \pi_s^+ D^0$  decay chains, with  $D^0 \rightarrow K^- \pi^+$  or  $D^0 \rightarrow K^- \pi^+ \pi^0$ . In the latter case, the  $\pi^0$  is not reconstructed. The  $\pi_s^+$  in the  $D^{*+}$  decay is known as the spectator pion and carries the sign of the charm quark. Vertexing techniques also cleanly isolate the mode  $D^+ \rightarrow K^- \pi^+ \pi^+$ . Both analyses benefit from the three-dimensional VXD information and the precise knowledge of the IP location.

In the  $D^{*+}$  kinematic analysis,  $D^0$  candidates are formed by cutting on the  $D^0$  invariant mass spectrum. For example, for the  $K\pi$  mode, the central value is  $1.765 \text{ GeV}/c^2 < m(K\pi^+) < 1.965 \text{ GeV}/c^2$ , and, for the "satellite" peak, we require  $1.50 \text{ GeV}/c^2 < m(K\pi^+) < 1.70 \text{ GeV}/c^2$ . A cut is made on the opening angle between the direction of the  $D^0$  candidate in the lab frame and the K in the rest frame of the  $D^0$ . After this cut, the remaining candidates are combined with a slow pion having the correct charge and  $p_\pi > 1.0 \text{ GeV}/c$ . Finally, we take advantage of the fact that  $c\bar{c}$  events are produced at high  $x_{D^*}$ , defined as  $2 \cdot E_{D^*}/E_{cm}$ , relative to background;  $x_{D^*}$  is required to be  $\geq 0.4$ .

For the  $D^{*+}$  vertex analysis, the emphasis is on the fact that  $D^0$ 's in  $c\bar{c}$  events have a significant three-dimensional decay length and are produced at the IP. The cuts on the opening angle and  $p_\pi$  are eliminated, and the  $x_{D^*}$  cut is reduced to  $x_{D^*} \geq 0.2$ .  $D^0$  tracks

are required to have a good three-dimensional vertex fit, with a three-dimensional decay length distinct from the IP by  $2.5 \sigma_L$ , where  $\sigma_L$  is the error on  $L$ . To assure that the direction of the  $D^0$  points to the IP, the two-dimensional impact parameter of the  $D^0$  to the IP is required to be  $< 20 \mu\text{m}$ . Together, the vertex and impact parameter cuts strongly reject combinatoric background and  $D^{*+}$  from beauty cascades.

A vertex-style analysis is used to isolate  $D^+ \rightarrow K^- \pi^+ \pi^+$  in  $\bar{c}$  events. A cut is made on the opening angle between the direction of the  $D^+$  candidate in the lab frame and the  $K$  in the rest frame of the  $D^+$ ;  $x_{D^+}$  is required to be  $\geq 0.4$ . The three-dimensional decay length measured from the IP is required to be at least  $3 \cdot \sigma_L$ . Finally, the angle between a line drawn from the  $D^+$  vertex to the IP and the direction of the  $D$  must be  $< 5 \text{ mrad}$  in the  $r$ - $\phi$  plane and  $< 20 \text{ mrad}$  in the  $r$ - $z$  plane.

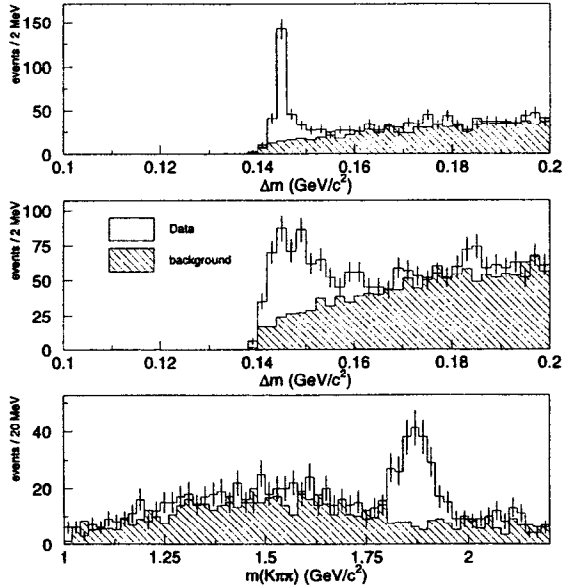


Figure 9. Distributions of the  $D^{*+} - D^0$  mass difference for  $D^0 \rightarrow K^- \pi^+$  (top) and  $D^0 \rightarrow K^- \pi^+ \pi^0$  (middle); and the  $D^+ \rightarrow K^- \pi^+ \pi^+$  mass (bottom).

Plots of the  $D^{*+} - D^0$  mass differences and the  $D^+ \rightarrow K^- \pi^+ \pi^+$  mass are shown in Fig. 9. A clean signal is extracted in each case. The signal region in the plots of the  $D^{*+} - D^0$  mass difference is taken to be  $\Delta m < 0.15 \text{ GeV}/c^2$ , and the sideband region used is  $0.16 \text{ GeV}/c^2 < \Delta m < 0.20 \text{ GeV}/c^2$ . The union of the two analyses is used to determine the asymmetry. The signal region in the mass plot for  $D^+ \rightarrow K^- \pi^+ \pi^+$  is

$1.8 \text{ GeV}/c^2 < m(K^- \pi^+ \pi^+) < 1.94 \text{ GeV}/c^2$ , while the sideband regions are  $1.64 \text{ GeV}/c^2 < m < 1.74 \text{ GeV}/c^2$  and  $2.0 \text{ GeV}/c^2 < m < 2.1 \text{ GeV}/c^2$ . The raw asymmetry is plotted in Fig. 10 as a product of the charge of the charm meson and  $\cos \theta_D$ , where  $\theta_D$  is the polar angle of the  $D$  meson momentum, separately for left- and right-handed electron polarization.

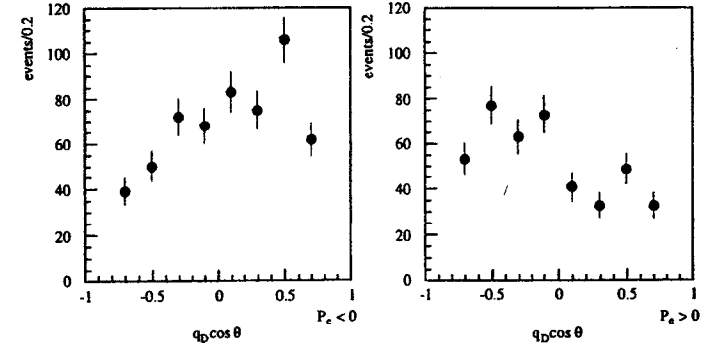


Figure 10. The raw asymmetry for the events in the signal mass region.

A maximum likelihood fit for the combined sample is used to extract  $A_c$ , taking into account the information on  $D^{(*)}$  momentum-dependent fractions of  $c\bar{c}$ ,  $b\bar{b}$  signal, and background components.  $A_c^D$  and  $A_b^D$  are the asymmetries from  $D^{(*)+}$  decays in tagged  $c\bar{c}$  and  $b\bar{b}$  events, respectively:

$$\ln L = \sum_{i=1}^n \ln \left\{ P_c^j(x_D^i) \left( \frac{1 - P_c A_c}{2(A_c - P_c)} (1 + y_i^2) + y_i A_c^D \right) + P_b^j(x_D^i) \left( \frac{1 - P_b A_b}{2(A_b - P_b)} (1 + y_i^2) + y_i A_b^D \right) + P_{RCBG}^j(x_D^i) (1 + y_i^2) + 2 A_{RCBG} y_i \right\}.$$

The preliminary result obtained is:

$$A_c = 0.64 \pm 0.11 \text{ (stat)} \pm 0.06 \text{ (sys)}.$$

The dominant systematics are related to the random combinatoric background (RCBG), as shown in Table 2; this is largely due to limited statistics in the sideband regions. Thus, the systematic errors can be expected to be reduced with a larger data sample.

Table 2

Systematic source	$\delta A_c$
RCBG fraction and acceptance	0.039
RCBG asymmetry	0.028
$c \rightarrow D/b \rightarrow D$ fraction	0.011
$b \rightarrow D$ asymmetry	0.022
b, c fragmentation	0.019
Beam polarization	0.007
QCD correction	0.007
Total systematic	0.058

### Measurement of $A_b$ , $A_c$ with Leptons

This analysis selects  $Z^0 \rightarrow c\bar{c}$  and  $b\bar{b}$  events with semileptonic decays. The analysis is an updated measurement based on the analysis of the 1993 data to include all 1993–1995 data.<sup>8</sup> Electrons are identified in the LAC by requiring agreement between the track momentum and the calorimeter electromagnetic energy, little or no calorimeter hadronic energy, and a reasonable front/back electromagnetic energy ratio. Muons are identified by comparing hits in the WIC with the extrapolated track, taking track extrapolation errors and multiple scattering into account. The lepton charge provides the quark anti-quark determination, and the quark direction is obtained from the jet nearest the lepton.

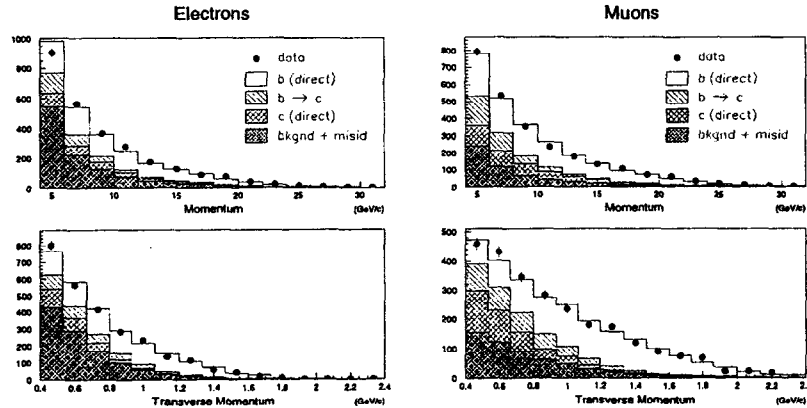


Figure 11. Distributions of momentum and transverse momentum with respect to the nearest jet axis for identified electrons (left) and muons (right) in the data (points) compared to the Monte Carlo prediction (histograms) for various sources.

$A_b$  and  $A_c$  are simultaneously extracted from the sample of leptons using a maximum likelihood fit of the identified leptons to the theoretical cross section, employing the distributions of the lepton momentum and transverse momentum. The Monte Carlo is used to estimate the composition of the lepton sample, determining the contributions to the observed asymmetry from all lepton sources and backgrounds. Fig. 11 shows a comparison of the lepton momentum and transverse momentum distributions between data and Monte Carlo separately for electrons and muons.

The preliminary result combining all our 1993 through 1995 muon and electron data is given below.

$$A_b = 0.87 \pm 0.07 \text{ (stat)} \pm 0.08 \text{ (syst)}$$

$$A_c = 0.44 \pm 0.11 \text{ (stat)} \pm 0.13 \text{ (syst)}.$$

A summary of the systematic errors and their sources are given in Table 3.

Table 3

Systematic source	$\delta A_b$	$\delta A_c$	Systematic source	$\delta A_b$	$\delta A_c$
Lepton mis-id rate	0.020	0.026	b-fragmentation	0.004	0.016
Background asymmetry	0.010	0.026	c-fragmentation	0.010	0.026
Jet axis simulation	0.043	0.030	$\text{Br}(b \rightarrow \bar{c} \rightarrow l)$	0.003	0.030
MC weights	0.032	0.032	$\text{Br}(b \rightarrow \tau \rightarrow l)$	0.002	0.015
Tracking efficiency	0.012	0.009	$\text{Br}(c \rightarrow l)$	0.003	0.023
$R_b = 0.218 \pm 0.002$	-0.006	0.006	$b \rightarrow l$ model	0.008	0.008
$R_c = 0.171 \pm 0.014$	0.006	-0.037	$c \rightarrow l$ model	0.037	0.042
$\chi = 0.120 \pm 0.010$	0.017	0.000	Beam polarization	0.011	0.006
$\text{Br}(b \rightarrow l) = 10.80 \pm 0.78\%$	-0.016	0.030	QCD correction	0.008	0.040
$\text{Br}(b \rightarrow c \rightarrow l) = 9.3 \pm 1.6\%$	0.011	-0.075	Total Systematic	0.078	0.132

Note that the systematic errors have begun to dominate the overall errors. In particular, systematic errors in semileptonic branching ratios produce a large contribution. Better knowledge in this area will lead to improvements in the final result.

### Self-Calibrated $A_b$ Measurement Using a Lifetime Tag and Momentum-Weighted Track Charge

The analysis utilizes an impact parameter tag to select an enriched sample of  $Z \rightarrow b\bar{b}$  events.<sup>9</sup> The direction of the primary b quark is determined by use of the net momentum-weighted track charge, a method first suggested by Feynman and Field, to assign the charge of the b quark.<sup>10</sup> An improved calibration technique reduces the model dependence involved in determining the analysis power of the momentum-weighted track charge method.<sup>11, 12</sup>



B events from the hadronic decay sample are tagged using tracking information from both the CDC and theVXD. The tracks were projected onto the plane perpendicular to the beam axis and the impact parameter measured relative to the IP. The distribution of the normalized two-dimensional impact parameter is shown in Fig. 12.

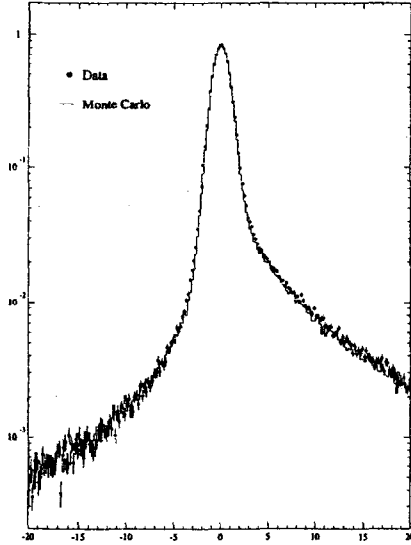


Figure 12. Distribution of the normalized impact parameter,  $d/\sigma_d$ .

B events are required to have  $\geq 3$  tracks at  $3\sigma$  in the two-dimensional impact parameter. This requirement is 61% efficient for tagging b events, giving a sample that is 89% pure. The event composition versus the number of tagging tracks at  $3\sigma$  is summarized in Fig. 13.

Next, the event is divided into two hemispheres along the thrust axis. The hemisphere momentum-weighted track charge difference is formed:

$$Q_{diff} = - \sum_{tracks} q_i \cdot \text{sgn}(\vec{p}_i \cdot \hat{T}) |\vec{p}_i \cdot \hat{T}|^K.$$

Here,  $\hat{T}$  is the thrust axis while  $q_i$  and  $p_i$  are the particle's charge and momentum, respectively. When  $Q_{diff}$  is  $> 0$ ,  $\hat{T}$  is taken to be the b quark direction.  $K$  is chosen so as to maximize the expression's sensitivity to the b quark direction and is set to the value of 0.5 for this analysis. Fig. 14 shows a comparison of the  $|Q_{diff}|$  distribution between data and Monte Carlo.

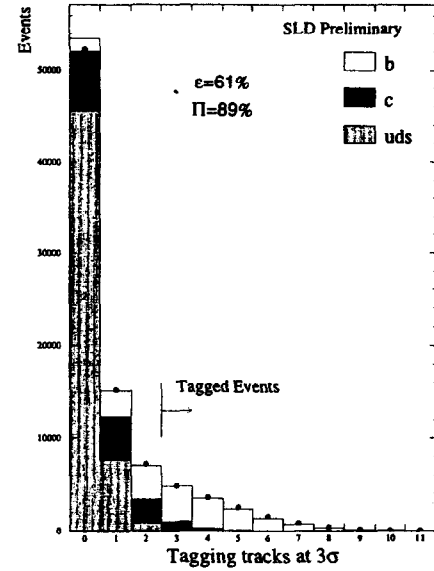


Figure 13. Event composition versus the number of tagging tracks at  $3\sigma$ .

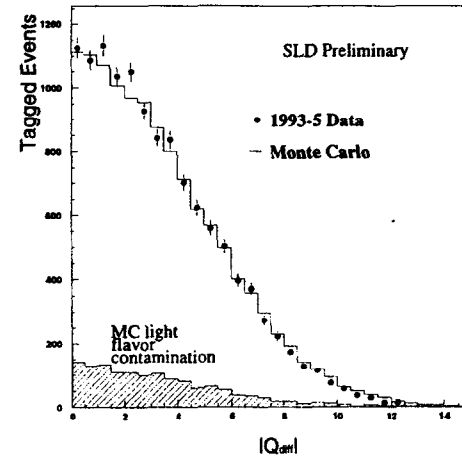


Figure 14. Comparison of the momentum-weighted charge  $|Q_{diff}|$  between data and Monte Carlo.

In order to extract  $A_b$ , a maximum likelihood fit is made to the b sample using the following probability distribution for each event  $i$ :

$$P_i = 1 + \cos^2 \theta_i + 2 \cos \theta_i \frac{A_e - P_e^i}{1 - A_e P_e^i} \left( \frac{f_b^i A_b (2P_{correct,b}^i - 1)(1 - \Delta_{QCD}^b(\cos \theta_i)) + f_c^i A_c (2P_{correct,c}^i - 1)(1 - \Delta_{QCD}^c(\cos \theta_i))}{(1 - f_b^i - f_c^i) A_{bkgnd} (2P_{correct,bkgnd}^i - 1)} \right).$$

The terms in the expression for the probability distribution include corrections,  $\Delta_{QCD}$ , for QCD effects that cause the direction of the final jet to differ from the initial direction of the quark, and the estimated asymmetry,  $A_{bkgnd}$ , from  $u\bar{u}$ ,  $d\bar{d}$ , and  $s\bar{s}$  decays of the Z.  $A_e$  is the asymmetry in the electron coupling to the Z,  $P_e^i$  is the polarization of the electron beam when the particular event was recorded, and  $f_{b(c)}^i$  is the probability that the particular event was a  $Z \rightarrow b\bar{b}$  ( $c\bar{c}$ ) decay.  $f_{b(c)}^i$  is parameterized as a function of the number of tracks missing the origin by  $3\sigma$ .  $P_{correct,b}^i$  and  $P_{correct,c}^i$  are the probabilities that the weighted momentum method has made the correct sign determination. Fig. 15 demonstrates that the sign determination is effective, showing the angular distribution of the signed thrust axis separately for left- and right-handed electron polarization.

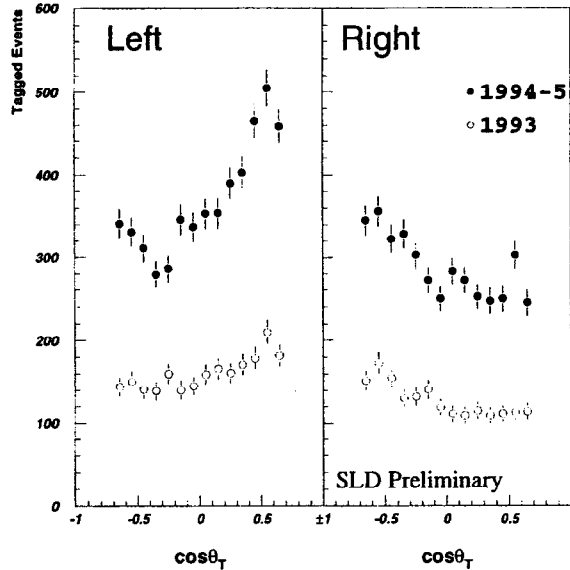


Figure 15. Distribution of the signed thrust axis in the 1993—1995 data sample.

$P_{correct,b}^i$  and  $P_{correct,c}^i$  are evaluated as a function of  $|Q_{diff}|$ . Both can be estimated from Monte Carlo, but  $P_{correct,b}^i$  can also be obtained from the data by using the information contained in the distribution of the difference of the hemisphere charges,  $Q_{diff}$ , defined above and in the distribution of the sum of the hemisphere charges,  $Q_s$ , defined below:

$$Q_s = \sum_{tracks} q_i \left( \vec{p}_i \cdot \hat{T} \right)^K.$$

The relevant quantities are found in the widths of the distributions of  $Q_s$  and  $Q_{diff}$ ,  $\sigma_s$  and  $\sigma_{diff}$ .  $Q_s$  and  $Q_{diff}$  are observables that are equivalent to the sum and difference of the momentum-weighted charges in the b-quark hemisphere,  $Q_b$ , and in the  $\bar{b}$ -quark hemisphere,  $Q_{\bar{b}}$ :

$$Q_s = Q_b + Q_{\bar{b}} \\ Q_{diff} = Q_b - Q_{\bar{b}}.$$

$P_{correct,b}^i$  is the fraction of time that  $Q_{diff} < 0$  as a function of  $|Q_{diff}|$ . With the assumption that the two hemisphere distributions are Gaussian and uncorrelated, the probability that the determination of the b-quark direction is correct is given by

$$P_{correct}(|Q_{diff}|) = \frac{1}{(1 + e^{-\alpha|Q_{diff}|})},$$

where  $\alpha$  is a function of  $\sigma_s$  and  $\sigma_{diff}$ :

$$\alpha = \frac{2 \sqrt{2 \left( \frac{\sigma_{diff}}{\sigma_s} - 1 \right)}}{\sigma_s}.$$

This expression is modified by hemisphere charge correlations due to overall charge conservation in the hadronization process and tracks which migrate from one hemisphere to the other. The result is a distortion of the joint probability of the two hemispheres from a circular Gaussian to a Gaussian ellipsoid, as illustrated in Fig. 16.

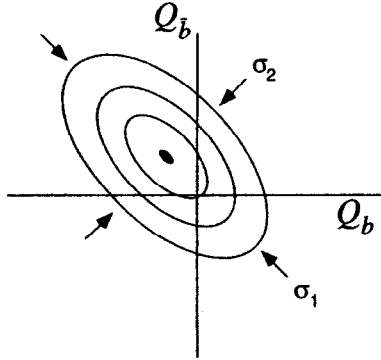


Figure 16. Effect of interhemisphere correlations on the momentum-weighted charge distributions.

The effect can be parameterized and a new expression for  $\alpha$  obtained which accounts for the correlation:

$$\alpha = \frac{2\sqrt{2\left(\frac{\sigma_{diff}}{(1+\lambda)\sigma_s} - 1\right)}}{(1+\lambda)\sigma_s}.$$

A comparison between the values for  $\alpha$ ,  $\sigma_s$ , and  $\sigma_{diff}$  for data and Monte Carlo are shown below. Note that  $\lambda$  is obtained from the Monte Carlo only.

Table 4

	Data	Monte Carlo
$\sigma_s$	$3.669 \pm 0.023$	$3.791 \pm 0.010$
$\sigma_{diff}$	$4.205 \pm 0.027$	$4.345 \pm 0.011$
$\lambda$	-	0.029
$\alpha$	$0.253 \pm 0.013$	$0.245 \pm 0.005$

The value for  $A_b$  obtained from the maximum likelihood fit is given below:

$$A_b = 0.843 \pm 0.046 \text{ (stat)} \pm 0.051 \text{ (sys)}.$$

The value is consistent with that expected for the SM. As can be seen from the final result, the measurement is limited by systematic errors. The systematics are dominated by the limitations of the self-calibration technique, first in the statistics of the data used to calculate  $\alpha$ , and second by our ability to calculate the effect of hemisphere charge correlations. A conservative estimate of the systematics due to our knowledge of the effects of charge correlations has been arrived at by varying the

fragmentation models employed in the Monte Carlo analysis; these include the JETSET string fragmentation model, the HERWIG 5.7 generator, and the independent fragmentation model. The range of variation among the models has been used for the range of error.

The systematic errors are summarized below. The uncertainty due to the  $\alpha_b$  calibration statistics will improve with larger data samples. Increased statistics and improved b selection criteria will also reduce the uncertainty due to the b-tag flavor composition. The issue of the hemisphere charge correlation will require further study before improvements can be made in the final result.

Table 5

Systematic Source	$\delta A_b/A_b$
$\alpha_b$ calibration statistics	3.4 %
P(Q) shape	1.0 %
$\cos\theta$ dependence of $\alpha_b$	1.5 %
hemisphere charge correlation	3.7 %
light flavor subtraction	0.2 %
c $\bar{c}$ analyzing power	0.2 %
b-tag flavor composition	2.6 %
$A_c = 0.67 \pm 0.07$	1.0 %
$A_{bkgd} = 0 \pm 0.50$	0.6 %
beam polarization	0.8 %
QCD correction	0.9 %
Total Systematic	6.2%

#### A New Measurement of $A_b$ with Tagged $K^\pm$

The analysis employs the fact that in the decay sequence  $\bar{B} \rightarrow D \rightarrow K^-$ , the identity of the b quark is given by the charge of the final state kaon.<sup>13</sup> Charged kaons are identified using the gas radiator of the SLD CRID. The analysis proceeds by selecting b events from the hadronic Z-decay sample using the two-dimensional impact parameter tag of the previous section. Events are then divided into hemispheres; in each hemisphere, tracks in the momentum range  $3 < p < 20$  GeV/c with an impact parameter in the  $r\phi$  plane  $> 1.5\sigma$  are selected.

These tracks are subjected to particle identification criteria which correspond to a K:  $\pi$  efficiency ratio of  $\sim 12 : 1$ . An event kaon charge sum is formed for the two event hemispheres:

$$Q_E = \sum_{Hemi=1}^{Hemi-1} Q_K - \sum_{Hemi=2}^{Hemi-2} Q_K.$$

If  $Q_E$  is less than zero, then the direction of hemisphere 1 is used for the direction of the b quark. Monte Carlo studies show that of the b events tagged by the impact parameter b tag, 30% will have a value of  $Q_E$  that is nonzero, and hence have the

direction of the  $b$  quark determined. Furthermore, of these events, 71% have the  $b$  quark direction assigned correctly.

The operation of the CRID detector is covered in the talk by R. Plano in these proceedings (see also Ref. [14]). As an example of the quality of the CRID particle ID information, Fig. 17 shows the Cherenkov radius vs. particle momentum for a small sample of tracks in the detector. The tagging efficiency of the CRID detector is calibrated by the use of  $\tau$  decays to find the probability that a pion could be misidentified as a kaon. One- and three-prong  $\tau$  decays provide a sample of pions (electrons and muons are not distinguished from pions) with a small, but well-known,  $K$  admixture. This study shows that 75% of the final candidates are kaons.

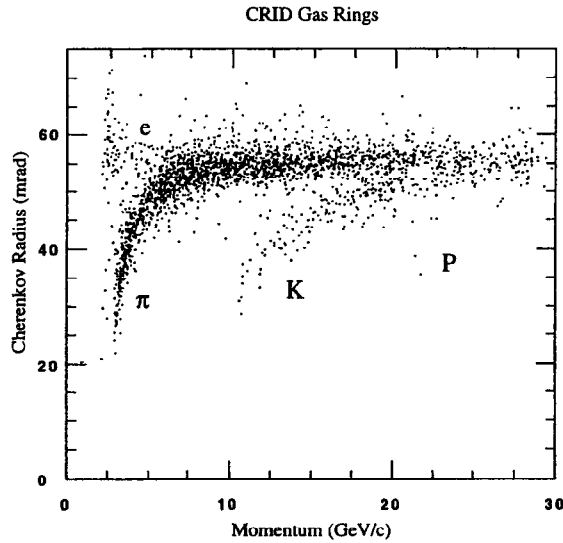


Figure 17. The measured Cherenkov radius versus particle momentum.

Figure 18 shows a comparison of the number of kaons per event for data and Monte Carlo. As a consistency check, one can compute the fraction of events with both hemispheres signed by kaons that have opposite sign. This is a good test of how well we understand the  $b$  quark correct signing probability. For data, this fraction is  $62.4 \pm 2.9\%$ , which can be compared to the value for Monte Carlo,  $61.9 \pm 1.5\%$ . With a larger data sample, the number of single and double hemisphere tags can be used to

calibrate the  $b$  quark direction tagging efficiency in a fashion similar to the analysis that extracted the  $b$  quark identification efficiency in the measurement of  $R_b$ .

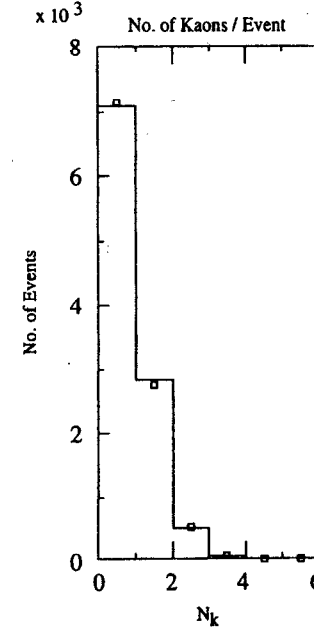


Figure 18. The number of kaons per event for data (points) and Monte Carlo (histogram).

The background subtracted asymmetry  $\tilde{A}_{data}^{corr}$  is formed as a function of  $\cos\theta$ . Monte Carlo  $b$  events are processed through the same analysis to form  $\tilde{A}_{MC}^b$ . The value for the  $A_b$  measurement is obtained by scaling  $\tilde{A}_{MC}^b$  to fit the data; the result is shown in Fig. 19. The fit effectively includes QCD corrections as in the JETSET MC. The preliminary  $K$ -tag result for  $A_b$  is

$$A_b = 0.91 \pm 0.09 \text{ (stat)} \pm 0.09 \text{ (sys)}.$$

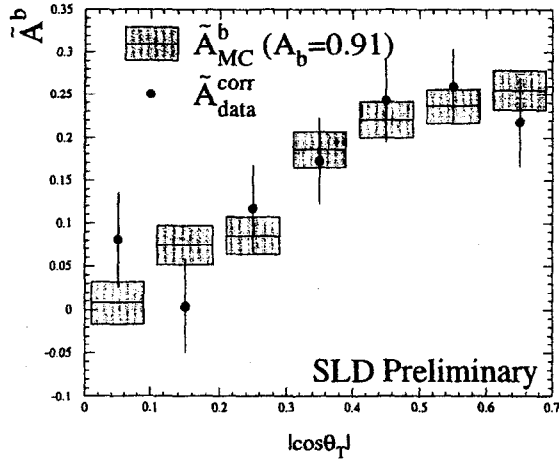


Figure 19. Distribution of the signed left-right forward-backward asymmetry.

A preliminary estimate of the systematics is given in Table 6. It should be noted that the majority of the detector and physics systematics associated with the uncertainty of the  $b$  event analyzing power can be understood with a calibration from the double-hemisphere charge comparison when statistics are sufficient for the task.

Table 6

Systematic Source	$\delta A_b/A_b$
kaon mis-id.	0.053
tracking efficiency	0.019
MC statistics	0.030
B production/mixing	0.040
B $\rightarrow$ D model	0.011
B vertex K yield	0.041
charm decay K yield	0.030
uds K production	0.011
b, c fragmentation	0.007
tag composition	0.002
$A_c = 0.666 \pm 0.070$	-0.014
beam polarization	0.007
QCD correction	0.009
Total Systematic	0.094

### $Zb\bar{b}$ Coupling Parity-Violation versus $\delta \sin^2 \theta_W^{eff}$

The preliminary SLD measurements presented here have been combined with a simultaneous fit to  $A_b$  and  $A_c$ , taking into account the systematic correlations between measurements. The combined SLD results are  $A_b = 0.858 \pm 0.054$  and  $A_c = 0.577 \pm 0.097$ , with a 12.3%  $A_b$ ,  $A_c$  correlation. The SM predictions are  $A_b = 0.935$  and  $A_c = 0.666$ . These results can be compared with the average LEP measurements:  $A_b = 0.884 \pm 0.032$  and  $A_c = 0.642 \pm 0.053$ , which are derived from the LEP  $A_{FB}^{0,b}$  and  $A_{FB}^{0,c}$  results<sup>15</sup> using  $A_e = 0.1506 \pm 0.0028$  from a combination of the SLD  $A_{LR}$  and LEP  $A_e$ .

Fig. 20 shows the complementary nature of a direct measurement of  $A_b$  to the electroweak measurements of  $\sin^2 \theta_W^{eff}$  and  $A_{FB}^b$ . The plot is made according to the scheme proposed by Takeuchi et al.<sup>16</sup>, which is discussed more fully in the review by M. Swartz in these proceedings. The deviations from the SM can be represented as a cross-section-like variable,  $\xi_b$ , and a parity-violation-like variable,  $\zeta_b$ , in addition to  $\delta \sin^2 \theta_W^{eff}$ . The allowed  $\zeta_b$  versus  $\delta \sin^2 \theta_W^{eff}$  bands for a number of current experimental results are shown in Fig. 20. The SM point at (0,0) is defined by  $m_t = 180 \text{ GeV}/c^2$ ,  $m_H = 300 \text{ GeV}/c^2$ ,  $\alpha_s = 0.117$ , and  $\alpha_{em} = 1/128.96$ . The thin horizontal band around (0,0) corresponds to the SM  $m_t$ ,  $m_H$  variations as indicated on the plot. The 68% and 90% CL contours for the best fit to all measurements are also shown.

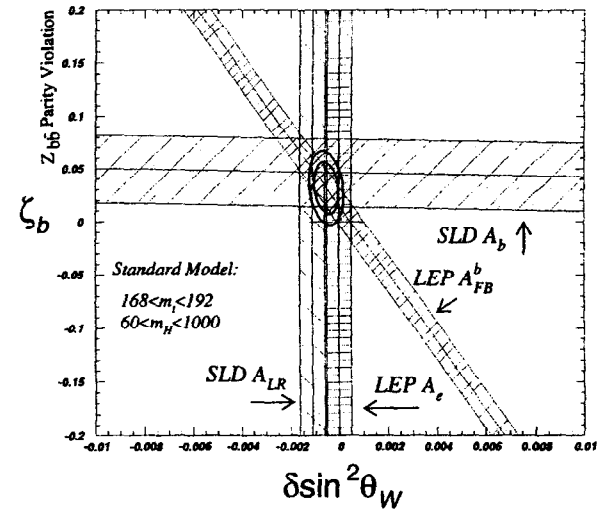


Figure 20.  $Zb\bar{b}$  coupling parity violation versus  $\delta \sin^2 \theta_W^{eff}$ .

## Measurements of the $B^+$ and $B^0$ Meson Lifetimes

In the naive version of the spectator model of heavy quark decays, the decay of the heavy quark proceeds independently of the accompanying light quarks. This means that different hadrons containing the same heavy quark should have the same lifetime. In the case of charm decays, this model did not work very well; experimental data gave a hierarchy of lifetimes instead, providing evidence for nonspectator processes. However, since these corrections scale as  $1/m_Q^2$ , the decays of  $b$  quarks should be less influenced by such effects and the lifetimes are expected to differ by less than 10%.<sup>17</sup> Consequently,  $B$  hadron lifetimes are expected to be useful for developing a better understanding of the fundamental heavy hadron decay mechanism. Moreover, the decay widths are important in that they normalize the rate determinations from which the CKM element  $V_{cb}$  is extracted. There are also more pedestrian reasons for interest in the  $B$  lifetimes; they are fundamental in determining the effect of cuts on decay lengths, and therefore their values feed into measurements of other heavy quark parameters.

SLD employs two complementary methods to extract these quantities.<sup>18</sup> Method 1 takes a semi-exclusive approach, restricting the sample to  $B$  hadron semileptonic decays. The advantage of this is that the vertices one works with are relatively clean. Method 2 takes a more inclusive, topological approach which searches for vertices in three-dimensional coordinate space. This method has the advantage of almost an order of magnitude increase in the number of decays available for analysis.

### Method 1: Semileptonic Analysis

A sketch of the topology of the decays we are looking for is shown in Fig. 21. The task is to bring together the separate pieces of the decay sequence. The topology of the  $B$  semileptonic decay modes provides a lookup table correlating the allowed net charge and number of prongs at both the  $B$  vertex and the  $D$  vertex with the charge of the original  $B$  particle.

High momentum electrons and muons are identified which have a high transverse momentum relative to the nearest jet axis. A search is made for a two-, three-, or four-prong  $D$  candidate vertex. A  $B$  vertex is formed by intersecting the  $D$  vertex momentum vector with the lepton. The  $D$  candidate decay length needs to be relatively large,  $> 4\sigma$ , relative to the IP, and the mass is required to be less than  $1.9 \text{ GeV}/c^2$ . An attempt is made to find a primary track which can be attached to the  $B$  vertex (this is done in order to attach slow transition pions from  $D^*$  decays.) Cuts are made on the resultant  $B$  vertex, requiring a mass  $> 1.4 \text{ GeV}/c^2$  (including the  $D$ ), and a decay length  $> 800$  microns. Finally, a set of  $B \rightarrow D$  linking cuts are made which depend on the topology of the candidate found. If a 1-prong  $B$  decay has been found, the distance of closest approach between the  $B$  vertex and the  $D$  momentum vector is required to be less than (130,100,70) microns for (two,three,four)-prong  $D$  vertices. For a two-prong  $B$  decay, the three-dimensional impact parameter between the  $D$  vector and the  $B$  vertex must be less than 200 microns.

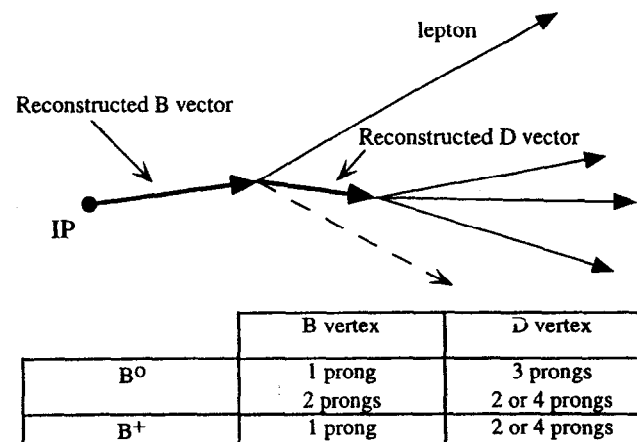


Figure 20. The decay topology in the semileptonic analysis.

The charge constraints at each vertex can be relaxed to provide a test of how well the kinematic selection is proceeding. Fig. 22 shows the number of 2-prong  $B$  vertices and two-, three-, and four-prong  $D$  vertices as a function of the net charge. The agreement between data and Monte Carlo is quite good. For example, the charge distribution for two-prong  $B$  vertices shows that the track associated with the lepton most often has the opposite charge, as expected. The clear excess at zero net charge, even after the size of the charge  $\pm 2$  wings is taken into account, is evidence that the selection criteria are functioning well.

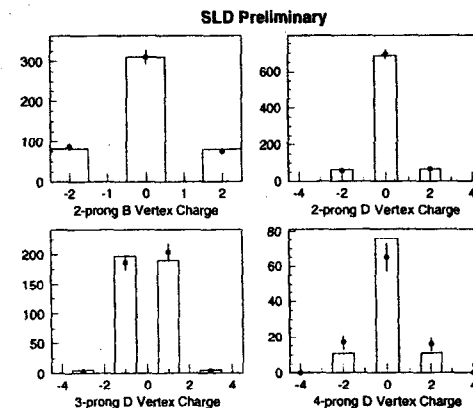


Figure 22. Comparison of the charge assignment between the data (points) and Monte Carlo (histogram) for the semileptonic analysis.

Similarly, a test of the quality of the data sample can be made by plotting the left-right forward-backward asymmetry for the final sample of B candidates. This is shown in Fig. 23 separately for the charged and the neutral B sample. The distribution shows good agreement between Monte Carlo and data asymmetries. The dilution of the asymmetry seen for the neutral B case is a result of  $B^0 - \bar{B}^0$  mixing. If the charge assignment were completely random, the charged and neutral cases would show the same asymmetry.

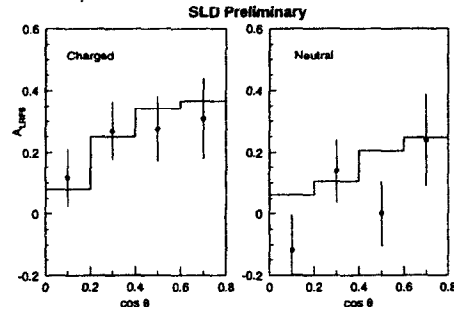


Figure 23. The left-right forward-backward asymmetry for charged and neutral decays in the semileptonic data for data (points) and Monte Carlo (histogram).

The purity and composition of the B sample for the semileptonic case is summarized in Table 7.

Table 7

	Neutral	Charged
$b\bar{b}$	98.7%	95.3%
$c\bar{c}$	1.1%	3.8%
$uds$	0.2%	0.9%
$B_u$	15.8%	70.1%
$B_d$	65.4%	18.4%
$B_s$	13.6%	4.1%
B baryons	3.9%	2.3%

The final sample consists of 428 neutral and 548 charged decays. The lifetime is extracted from the decay length distribution of the secondary vertices using a binned maximum likelihood technique. Simultaneous maximum likelihood fits were made to the charged, to neutral lifetime ratio  $R$ , and either the charged or the neutral lifetime. Plots of the decay lengths for neutral and charged events comparing data and the MC

best fit are shown in Fig. 24. The preliminary results for the lifetime ratio and the charged and neutral lifetimes are:

$$R = \tau^\pm / \tau^0 = 0.94^{+0.14}_{-0.12} (\text{stat}) \pm 0.07 (\text{sys})$$

$$\tau_{B^0} = 1.60^{+0.15}_{-0.14} (\text{stat}) \pm 0.10 (\text{sys}) \text{ ps}$$

$$\tau_{B^\pm} = 1.49^{+0.11}_{-0.10} (\text{stat}) \pm 0.05 (\text{sys}) \text{ ps}.$$

The systematic errors will be described below (see also Table 9).

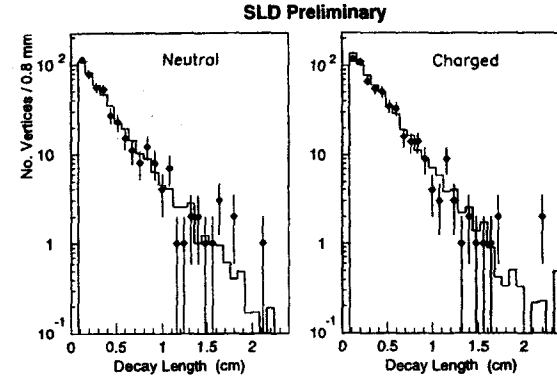


Figure 24. Decay length distributions for charged and neutral decays in the semileptonic analysis for data (points) and the best fit Monte Carlo (histogram).

## Method 2: Topological Approach

Initially, a sample of  $b\bar{b}$  events is selected with the two-dimensional impact parameter tag described previously. In this analysis the strategy is to search for vertices in three-dimensional coordinate space. Each track  $i$  is associated with a function  $f_i(r)$  representing a Gaussian probability "tube" for the track trajectory. The goal is to find those locations in space with a maximum summed probability; a vertex function which can serve this purpose is defined for a point in space  $r$ :

$$V(r) = \sum_i f_i(r) - \frac{\sum_i f_i^2(r)}{\sum_i f_i(r)}.$$

The projections of the track functions and, separately, the vertex function onto the xy plane are shown in Fig. 25 for a sample event. A close look at the vertex function shows two peaks. One is at the location of the IP, and the second isolates a secondary-decay vertex.

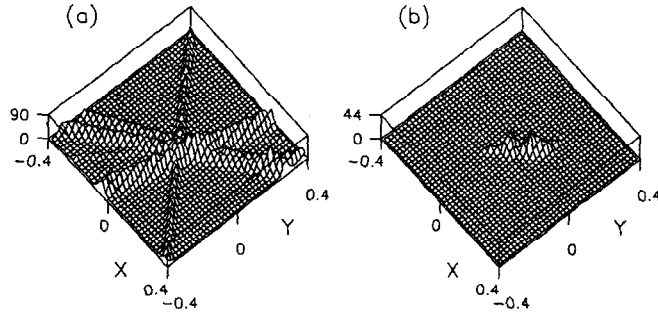


Figure 25. (a) The track and (b) the vertex functions projected onto the xy plane.

The secondary vertex is used as a seed location. Additional tracks are added to the original vertex; here, optimization of the charge reconstruction as indicated by the Monte Carlo is the primary concern. A vertex axis is formed by drawing a line between the IP and the seed vertex, and the distance between the IP and the seed vertex,  $D$ , determined. The transverse impact parameter,  $T$ , and the corresponding distance along the vertex axis,  $L$ , are calculated for all candidate tracks. Those with small  $T$  and large  $L/D$  are likely to be associated with the seed location. Good quality tracks with  $T < 0.1$  cm and  $L/D > 0.3$  are added to the initial set of tracks forming the secondary vertex.

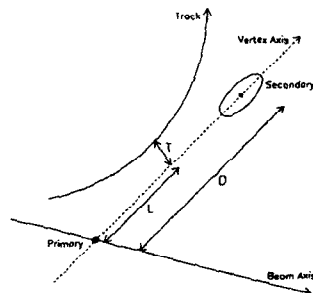


Figure 26. Impact parameter of a track with respect to the seed vertex axis.

Two cuts on the fully reconstructed secondary vertex are made. The first requires that the mass of the fully reconstructed secondary vertex be greater than  $2 \text{ GeV}/c^2$ . The quark composition of the secondary vertex is shown as a function of the vertex mass for both neutral and charged vertices in Fig. 27. After the mass cut, the neutral sample is 99.3%  $b\bar{b}$  and the charged sample 99.0%  $t\bar{b}$ . Note that a clear  $K^0$  peak can be seen in the neutral distribution. The second cut demands that the minimum decay length of the secondary vertex be greater than 1 millimeter. This is to minimize confusion with tracks originating from the IP.

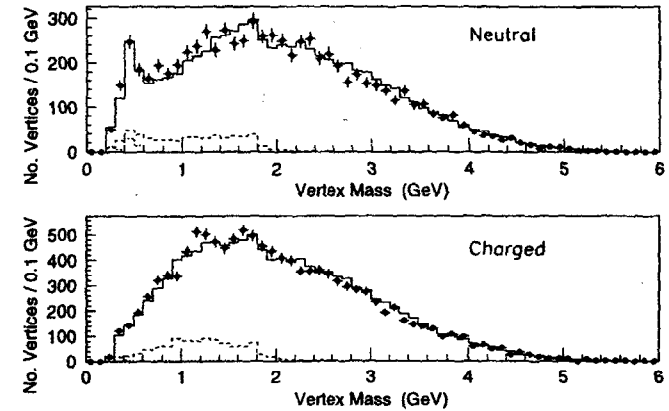


Figure 27. Mass of reconstructed secondary vertices for charged and neutral decays in the topological analysis. The dashed (dotted) histograms represent the charm (uds) contribution from Monte Carlo.

The neutral sample consists of the hemispheres with secondary vertex charge equal to zero, while the charged sample consists of those with a secondary vertex charge equal to  $\pm 1$ ,  $\pm 2$ , or  $\pm 3$ . Fig. 28 illustrates the sample composition as a function of the charge of the reconstructed vertices. The distribution of the reconstructed charge shows good agreement between data and Monte Carlo. The information is summarized in Table 8.

Table 8

	Neutral ( $Q=0$ )	Charged ( $Q=\pm 1, \pm 2, \pm 3$ )
Bu	22.2%	56.2%
Bd	55.5%	29.8%
Bs	15.3%	8.2%
B baryons	6.3%	4.8%



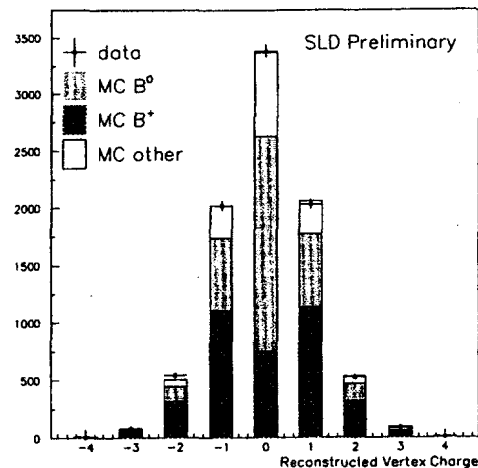


Figure 28. Distribution of charges reconstructed by the topological analysis.

A further test can be made for the charged sample. Fig. 29 shows the distribution of  $\cos\theta$  between the event thrust axis (used as the best estimator of the original  $b$  quark direction) and the positron direction signed by the product of the electron polarization and the reconstructed vertex charge. Neutral  $B$  decays with the wrong charge assignment would cause a dilution of the observed asymmetry and flatten the distribution as a function of  $\cos\theta$ . Again, there is good agreement between data and Monte Carlo.

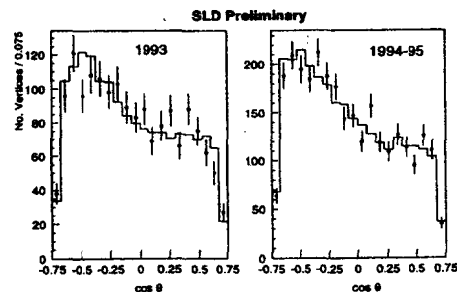


Figure 29. Distribution of the event thrust axis with respect to the positron beam, signed by the product of electron polarization and reconstructed charge for data (points) and Monte Carlo (histogram).

The final sample contains 3382 neutral and 5303 charged decays. Simultaneous maximum likelihood fits were made to the lifetime ratio  $R$  and either to the charged or the neutral lifetime. Plots of the decay lengths for neutral and charged events comparing data and the MC best fit are shown in Fig. 30. The preliminary results for the lifetime ratio and the charged and neutral lifetimes are:

$$R = \tau^{\pm}/\tau^0 = 1.08^{+0.09}_{-0.08} (\text{stat}) \pm 0.10 (\text{sys})$$

$$\tau_{B^0} = 1.55 \pm 0.07 (\text{stat}) \pm 0.12 (\text{sys}) \text{ ps}$$

$$\tau_{B^{\pm}} = 1.67 \pm 0.06 (\text{stat}) \pm 0.09 (\text{sys}) \text{ ps.}$$

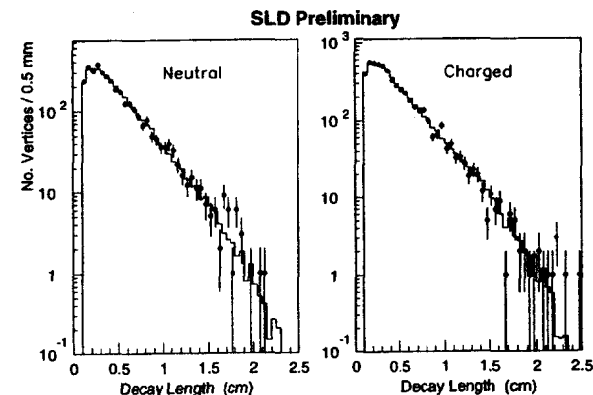


Figure 30. Decay length distributions for neutral and charged decays in the topological analysis for data (points) and the best fit Monte Carlo (histogram).

The systematic errors for both the semileptonic and the topological analyses are summarized in Table 9. The main contribution to the systematic error due to detector modeling originates from the uncertainty in the track reconstruction efficiency. Contributions to the systematic error due to physics modeling include the uncertainties in the  $b$  quark fragmentation and the  $B$  meson decay model, as well as the sensitivity to assumptions concerning  $B_s$  and  $B$  baryon production and lifetimes. The largest contribution to the systematic error arises from uncertainties in the fitting procedure and also from Monte Carlo statistics in the semileptonic analysis. The fitting uncertainties were conservatively estimated by varying the bin size used in the decay length fit distributions, and by modifying the cuts on the minimum and/or maximum decay lengths used in the fit.

Table 9

Systematic error	Semileptonic			Topological		
	$\Delta\tau_{B^*}$ (ps)	$\Delta\tau_{B^0}$ (ps)	$\Delta(\tau'/\tau^0)$	$\Delta\tau_{B^*}$ (ps)	$\Delta\tau_{B^0}$ (ps)	$\Delta(\tau'/\tau^0)$
Detector Modeling						
Charge assignment	0.004	0.016	0.014	0.040	0.040	0.040
Lepton ID	0.001	0.006	0.002	-	-	-
Physics Modeling						
b fragmentation	0.056	0.026	0.022	0.032	0.032	<0.005
B decay charm	0.009	0.006	0.007	<0.005	0.020	0.020
BR(B $\rightarrow$ D**/vX)	0.011	0.004	0.006	-	-	-
B decay multiplicity	0.011	0.015	0.016	0.010	0.030	0.030
B <sub>s</sub> fraction	0.006	0.004	0.005	0.005	0.019	0.010
B baryon fraction	0.014	0.004	0.007	0.021	0.014	0.006
B <sub>s</sub> lifetime	0.029	0.001	0.017	0.053	0.013	0.051
B baryon lifetime	0.005	0.002	0.003	0.016	0.004	0.012
B $\rightarrow$ D spectrum	-	-	-	0.025	0.006	0.019
Charm hadron $\tau$	0.011	0.001	0.007	-	-	-
Monte Carlo and Fitting						
Fit systematics	0.060	0.010	0.040	0.087	0.057	0.056
MC statistics	0.042	0.030	0.039	0.021	0.018	0.027
TOTAL	0.100	0.047	0.068	0.122	0.091	0.100

### Summary

We have presented preliminary SLD results on heavy quark physics which are competitive with the current world measurements. The future holds promise for further progress in the precision and scope of the SLD analyses, with advances coming on a number of fronts. The schedule for SLD data running calls for an additional 500,000 Z decays at  $\sim 80\%$  electron polarization, providing a factor of four increase in statistics over the present data sample. An upgraded CCD vertex detector has been installed prior to the January 1996 SLD run.<sup>19</sup> The new detector provides improved solid angle coverage ( $\langle \cos\theta \rangle_{\max} = 0.75 \rightarrow \langle \cos\theta \rangle_{\max} = 0.85$ ), overlapping three-layer CCD coverage, and an increased lever arm, all of which result in significantly improved resolution and efficiency. Finally, new analysis techniques promise to take better advantage of the analyzing power provided by the small IP spot size, the vertex detector, and the electron polarization.<sup>20</sup> Taken together, these developments should open new, exciting possibilities for physics at SLD.

### Acknowledgments

We thank the personnel of the SLAC Accelerator Department for their outstanding achievements in bringing micrometer-size beams into collision at the SLD with remarkable reliability.

### REFERENCES

- 1) G. Agnew *et al.*, SLD Design Report, SLAC-0273 (1984).
- 2) VXD: G. Agnew *et al.*, SLAC-PUB-5906 (1992); CDC: M. Hildreth *et al.*, SLAC-PUB-6656 (1994).
- 3) M. E. Peskin and T. Takeuchi, *Phys. Rev. D* **46**, 381 (1992).  
M. Swartz, "Tests of the Electroweak Standard Model," in Proceedings of the XVIth International Symposium on Lepton and Photon Interactions, Ithaca, NY, 1993, edited by P. Drell and D. Rubin, pp. 381-424.
- 4) SLD Collab.: K. Abe *et al.*, SLAC-PUB-7004, contribution to the International Europhysics Conference on High Energy Physics (HEP95).
- 5) ALEPH Collab.: D. Buskulic *et al.*, *Phys. Lett. B* **313**, 535 (1993).
- 6) A. Blondel, B. W. Lynn, F. M. Renard, and C. Verzegnassi, *Nucl. Phys. B* **304**, 438 (1988).
- 7) SLD Collab.: K. Abe *et al.*, SLAC-PUB-6681, submit. to *Phys. Rev. Lett.*
- 8) SLD Collab.: K. Abe *et al.*, *Phys. Rev. Lett.* **74**, 2895 (1995).
- 9) SLD Collab.: K. Abe *et al.*, SLAC-PUB-6569, 1995, submit. to *Phys. Rev. D*.
- 10) R. D. Field and R. P. Feynman, *Nucl. Phys. B* **136**, 1 (1978).
- 11) SLD Collab.: K. Abe *et al.*, *Phys. Rev. Lett.* **74**, 2890 (1995).
- 12) SLD Collab.: K. Abe *et al.*, SLAC-PUB-6979, contribution to the International Europhysics Conference on High Energy Physics (HEP95).
- 13) SLD Collab.: K. Abe *et al.*, contribution (EPS0251) to the International Europhysics Conference on High Energy Physics (HEP95).
- 14) K. Abe *et al.*, "Results from the SLD Barrel CRID Detector," published in *IEEE Trans. Nucl. Sci.* **41**: 862 (1994).
- 15) A. Olchevski, "Precision Tests of the Standard Model," in *Proceedings of the International EuroPhysics Conference on High Energy Physics* (Brussels, 1995).
- 16) T. Takeuchi, A. Grant, and J. Rosner, *Fermilab-Conf-94/279-T*.
- 17) I. I. Bigi *et al.*, in *B Decays*, ed. by S. Stone, World Scientific (1994).
- 18) SLD Collab.: K. Abe *et al.*, SLAC-PUB-6972, "Preliminary Measurements of B<sup>0</sup> and B<sup>+</sup> Lifetimes at SLD," contributed paper to LP'95: The International Symposium on Lepton-Photon Interactions (Beijing, China, August 10-15, 1995).
- 19) J. Brau, SLAC-PUB-7070, "VXD3: the SLD Vertex Detector Upgrade Based on a 307 MPixel CCD System," presented at the Nuclear Science Symposium (NNS) (San Francisco, CA, October 21-28, 1995).
- 20) For example, see E. Etzion, SLAC-PUB-7170, "Measurement of R<sub>b</sub> at SLD," paper presented at the Moriond Electroweak Conference, 1996.